Electronic Supplementary Information

Stacking Polytypes of 1T′ Phase Se-Rich Transition Metal Diselenide and Their Electrocatalytic Activity of Hydrogen Evolution Reaction

Ju Yeon Kim[‡a] In Hye Kwak, [‡ab] Ik Seon Kwon,[‡ab] Qadeer Akbar Sial,[a] Junaid Ihsan,[a]

Getasew Mulualem Zewdie,[c] Jeunghee Park,*[a] and Hong Seok Kang*[d]

[a] Department of Advanced Materials Chemistry, Korea University, Sejong 339-700, Republic of Korea; *E-mail: parkjh@korea.ac.kr.

[b] Pohang Accelerator Laboratory, POSTECH, Pohang 37673, Republic of Korea

[c] Institute for Application of Advanced Materials, Jeonju University, Chonju, Chonbuk 55069, Republic of Korea

[d] Department of Nano and Advanced Materials, Jeonju University, Chonju, Chonbuk 55069, Republic of Korea; *E-mail: hsk@jj.ac.kr

[‡] J. Y. Kim, I. H. Kwak, and I. S. Kwon equally contribute as the first author.

Contents

Computation and Experimental Section

Table S1. Parameters of pristine $MoSe_2$ and WSe_2.

Table S2. Parameters of Model I for $MoSe_x$ and WSe_x.

Table S3. Parameters of Model S for $MoSe_x$ and WSe_x.

Table S4. Parameters of Model C for $MoSe_x$ and WSe_x.

Table S5. Comparison of HER performance with the previous works.

I. Computation and Experimental Section

Computation. First-principles calculations were performed through spin-polarized density functional theory (DFT) to investigate how the excess Se atoms changes the phase from 2H to 1T′ polytypes. The Vienna *Ab-initio* Simulation Package (VASP) is mainly used for this calculation.[S1,S2] The electron-ion interactions were described using the projector-augmented wave (PAW) method with a plane-wave kinetic energy cutoff of 400 eV.[S3] The effect of attractive van der Waals (vdW) interaction was taken into account by employing Grimme's D3 correction (PBE-D3).[S4] Structural optimization was performed until the average force was < 0.03 eV·Å^{-1}. Both ionic and lattice relaxation was performed using the PBE-D3 exchange-correlation functional. Monkhorst-Pack *k*-point sampling of 3×3×3 was used for the geometry optimization.

For the slab geometry, a vacuum space of 20 Å was used along the *Z* (//*c*) direction (perpendicular to the slabs) to ensure that there is no noticeable interaction between periodic images of slabs. The Methfesser-Paxton method with a broadening of 0.1 eV is used for slabs. Total energy of a system was taken by extrapolating the smearing parameter to zero K. The convergence with respect to SCF was attained when the total-energy change between cycles is less than $1×10^{-6}$ eV. A Monkhorst-Pack *k*-point sampling of 3×3×1 was used. The change in Gibbs free energy (ΔG) during the reaction provides useful information about the energy and spontaneity of the reaction (whether it can happen without additional energy).

Under standard conditions, the HER consists of two steps, the adsorption of H on the catalyst in the Volmer reaction (*), followed by the Heyrovsky/Tafel reaction to release hydrogen molecules ($1/2\ H_2$ + *). Therefore, we should construct the Gibbs free energy profile along the reaction coordinate by calculating the relative free energies of the reactant and intermediates in the Volmer reaction. The ΔG can be calculated according to the equation;[S5]

$\Delta G = \Delta E_{DFT} + \Delta E_{ZPE} + \Delta H_{corr} - T\Delta S$, where E_{DFT} is the total energy of hydrogen atom adsorption calculated from DFT, ΔE_{ZPE} is the zero point energy change, ΔH_{corr} is H-correction, i.e. the reaction enthalpy change from 0 to 298 K, and $T\Delta S$ is the entropy change between adsorbed hydrogen and hydrogen in the gas phase under standard conditions, based

$$H_{corr} = \int_{0}^{298} C_V dT$$

on the Debye model. was calculated from the vibrational heat capacity using the calculated vibrational frequencies by Harmonic Approximation.[S6] The H_2 molecule is treated as an ideal gas, while the adsorbed H is treated using the harmonic approximation. VASP calculations were used to determine the vibrational frequencies of adsorbed H atom on the system.

Synthesis. Most of chemicals were purchased from Signa-Aldrich and Alfa-Aesar Co. The TMD nanosheets were prepared using a hot injection colloidal synthetic route. The synthetic procedure was conducted using Schlenk line under Ar flow, following the four steps.

Step 1: 5 mL of oleylamine (OAm; $C_{18}H_{35}NH_2$; molecular weight (MW) = 267.493 g mol^{-1}, technical grade 70%, density = 0.813 g mL^{-1}) in a three-necked flask was degassed at 120 °C for 30 min, then the temperature was raised to 220-300 °C.

Step 2: 0.5 mmol of MoCl$_5$ (MW = 273.21 g mol^{-1}, 99.9%) or WCl$_6$ (MW = 396.5 g mol^{-1}, 99.9%) and 0.5-2 mmol of (PhCH$_2$)$_2$Se$_2$ (dibenzyl diselenide; MW = 340.2 g mol^{-1}, 95%) were dissolved in 5 mL OAm and the mixture was kept at 70 °C for 1 h.

Step 3: 2 mL of precursor solution was injected into the OAm solution in flask (prepared with an injection rate of 0.4 mL min^{-1} for 5 min, and the mixture was stirred at 220-300 °C for another 30 min. Total reaction time is 1 h.

Step 4: The reaction solution was cooled down to room temperature and the black products was separated by centrifugation. The products were washed with 1:1 ethanol:toluene mixed solvent for four times, and dried using an evaporator. For annealed samples, the product (powders) was placed in a quartz tube inside electrically heated furnace and annealed under Ar flow (flow rate

= 200 sccm) at 400 °C for 1 h.

Characterization. The products were characterized by high-resolution scanning electron microscopy (SEM, Jeol), field-emission transmission electron microscopy (FE TEM, Libra 200 MC TEM, Carl Zeiss), and high-voltage transmission electron microscopy (HV-TEM, Jeol JEM ARM 1300S, 1.25 MV). Energy-dispersive X-ray fluorescence spectroscopy (EDX) with elemental maps was measured using an Ultra Corrected Energy Filtering TEM operated at 200 kV that equipped with ZrO/W-field emitter system (Schottky emitter), EDX detector system (X-Max 80T, Oxford), and side CCD camera (ORIUS SC200D. Gatan). Fast Fourier-transform (FFT) images were generated by the inversion of the TEM images using Digital Micrograph GMS1.4 software (Gatan Inc.). High-resolution X-ray diffraction (XRD) patterns were obtained using the 3D and 9B beamlines of the Pohang Light Source (PLS)-II with monochromatic radiation ($\lambda = 1.52150$ Å). XRD pattern measurements were also carried out in a Rigaku D/MAX-2500 V/PC using Cu K_{α} radiation ($\lambda = 1.54056$ Å).

Electrochemical Measurements. Experiments were carried in a three-electrode cell connected to an electrochemical analyzer (CompactStat, Ivium Technologies). HER electrocatalysis in 0.5 M H_2SO_4 electrolyte was measured using a linear sweeping from 0 to -0.6 V (vs. RHE) with a scan rate of 2 mV s^{-1}. A saturated calomel electrode (SCE, KCl saturated, Pine Instrument) was used as a reference electrode. A Pt coil (with fritted glass) was used as a counter electrode. The electrolyte was purged with H_2 (ultrahigh grade purity 99.999%) during the measurement. The Pt counter electrode was encapsulated with a fritted glass tube, so that the Pt deposition on the working electrode was prevented.

The applied potentials (E) reported in our work were referenced to the reversible hydrogen electrode (RHE) through standard calibration as described elsewhere. We calibrate the potential of the reference electrode *vs.* standard hydrogen electrode (SHE). Cyclic voltammetry (CV) curves were obtained at a scan rate of 2 mV s^{-1}, in the high-purity H_2 saturated electrolyte with a Pt wire as the working electrode. The average value of the potential at which the current crossed at zero was -0.278 V. Therefore E (*vs.* RHE) = E (*vs.* SCE) + 0.278 V.

4 mg sample was mixed with 1 mg carbon black (Vulcan XC-72) dispersed in Nafion (20 μL) and isopropyl alcohol (0.98 mL). The catalyst materials (0.39 mg cm^{-2}) were deposited on a glassy carbon rotating disk electrode (RDE, area = 0.1963 cm^2, Pine Instrument),), and a rotation speed of 1600 rpm was used for the linear sweep voltammetry (LSV) measurements. The Pt/C (20 wt.% Pt in Vulcan carbon black, Sigma-Aldrich) tested as reference sample using

the same procedure. The LSV curves were reproducible for four separate loadings of samples on the GC RDE electrode.

Electrochemical impedance spectroscopy (EIS) measurements were carried out for the electrode in an electrolyte by applying an AC voltage of 10 mV in the frequency range of 100 kHz to 0.1 Hz at a bias voltage of -0.25V (vs. RHE). To measure double-layer capacitance via CV, a potential range in which no apparent Faradaic processes occur was determined from static CV. All measured current in this non-Faradaic potential region is assumed to be due to double-layer capacitance. The charging current, i_c, is then measured from CVs at multiple scan rates. The working electrode was held at each potential vertex for 10 s before beginning the next sweep. The charging current density (i_c) is equal to the product of the scan rate (v) and the electrochemical double-layer capacitance (C_{dl}), as given by equation $i_c = v\, C_{dl}$. The difference ($\Delta J_{0.15}$) between the anodic charging and cathodic discharging currents measured at 0.15 V or 0.05 V (vs. RHE) was used for i_c. Thus, a plot of $\Delta J_{0.15}$ as a function of v yields a straight line with a slope equal to $2 \times C_{dl}$. The scan rates were 20–100 mV s^{-1}.

To estimate the actual electrochemical surface area (ESCA), we used the C_{dl} value. The roughness factor (= ECSA) is defined as the surface area ratio between the catalyst and the flat TMD electrodes. This can be obtained using $\dfrac{C_{dl}}{C_s}$, where C_{dl} and C_s are electrochemical double-layer capacitance of the catalysts (measured by the procedure described above) and the flat surface, respectively. The C_s value is assumed to be 0.060 mF cm^{-2} for all samples.[S7] The specific surface of the electrode can be estimated by multiplying the geometrical surface (A_{geom} = 0.1963 cm^2) to ECSA; $A_{geom} \times$ ECSA.

Table S1. Parameters of two layered (4×4×1) supercells for pristine MoSe$_2$ and WSe$_2$.

	Phase	Lattice constants		E_{rel}^{tot} (eV)[a]	E_{rel} (meV)[b]
		a, b, c (Å)	α, β, γ (°)		
MoSe$_2$	2H	13.18, 12.99	90, 90, 120	0	0
	2M	11.95, 13.15, 13.47	90, 113.13, 90	11.23	116.9
	1T′	13.60, 13.06, 12.98	90, 90, 119	11.87	123.6
	T$_d$	11.93, 13.12, 12.75	90, 90, 90	10.90	113.5
WSe$_2$	2H	13.16, 12.99	90, 90, 120	0	0
	2M	11.87, 13.17, 13.68	90, 109.66, 90	9.89	103.0
	1T′	13.58, 13.12, 13.11	90, 90, 119	10.68	111.2
	T$_d$	11.88, 13.17, 12.86	90, 90, 90	9.63	100.3

[a] Relative total energy of the supercell, defined as $E_{2M \text{ (or 1T′, Td)}} - E_{2H}$.

[b] Relative energy per atoms, defined as E_{rel}^{tot} divided by the number of atoms.

Table S2. Parameters of two layered (4×4×1) supercells for Se-intercalated MoSe$_x$ and WSe$_x$ models.

(a) MoSe$_x$

x	Phase	a, b, c (Å)	α, β, γ (°)	E_{rel}^{tot} (eV)[a]	E_{rel} (meV)[b]	E_{int} (eV)[c]
2.06	2H	13.21, 14.22	90, 90, 120	0	0	2.01
	2M	11.96, 13.09, 14.57	90, 113.43, 90	8.02	81.8	0.41
	1T′	13.60, 13.08, 13.81	90, 90, 119	8.87	90.5	0.51
	T$_d$	11.97, 13.07, 13.59	90, 90, 90	8.49	86.6	0.81
2.13	2H	13.21, 15.35	90, 90, 120	0	0	1.29
	2M	12.00, 13.07, 15.25	90, 113.76, 90	6.75	67.5	0.17
	1T′	13.62, 13.18, 14.26	90, 90, 119	6.97	69.7	0.07
	T$_d$	12.01, 13.11, 14.33	90, 90, 90	7.33	73.3	0.40
2.25	2H	13.18, 16.28	90, 90, 120	0	0	0.72
	2M	11.99, 13.36, 17.25	90, 120.58, 90	3.04	29.2	-0.31
	1T′	13.72, 13.33, 14.94	90, 90, 119	4.77	45.8	-0.17
	T$_d$	12.02, 13.36, 14.81	90, 90, 90	3.19	30.7	-0.25

(b) WSe$_x$

x	Phase	a, b, c (Å)	α, β, γ (°)	E_{rel}^{tot} (eV)[a]	E_{rel} (meV)[b]	E_{int} (eV)[c]
2.06	2H	13.18, 14.29	90, 90, 120	0	0	2.36
	2M	11.93, 13.12, 14.82	90, 113.42, 90	6.48	66.1	0.66
	1T′	13.59, 13.14, 13.85	90, 90, 119	7.29	74.3	0.67
	T$_d$	11.92, 13.12, 13.69	90, 90, 90	6.96	71.2	1.03
2.13	2H	13.18, 15.59	90, 90, 120	0	0	1.60
	2M	11.95, 13.15, 15.41	90, 114.22, 90	4.68	46.8	0.29
	1T′	13.65, 13.22, 14.45	90, 90, 119	5.35	53.5	0.26
	T$_d$	11.94, 13.18, 14.63	90, 90, 90	5.41	54.1	0.54
2.25	2H	13.17, 16.35	90, 90, 120	0	0	0.89
	2M	11.98, 13.32, 15.54	90, 102.61, 90	2.57	24.7	-0.03
	1T′	13.72, 13.40, 14.99	90, 90, 119	3.64	35.0	0.01
	T$_d$	11.99, 13.40, 14.86	90, 90, 90	1.75	16.8	-0.10

[a] Relative total energy of the supercell, defined as $E_{2M \text{ (or 1T', Td)}} - E_{2H}$.

[b] Relative energy per atoms, defined as E_{rel}^{tot} divided by the number of atoms.

[c] Se intercalation energy (per Se), defined as $E_{int} = [E(MoSe_x \text{ or } WSe_x) - E(MoSe_2 \text{ or } WSe_2) - n\mu(Se)]/n$ for the intercalation reaction of MoSe$_2$ (or WSe$_2$) + nSe → MoSe$_x$ (or WSe$_x$). E is the total energy of the model, n is the number of Se atoms, and μ(Se) is the chemical potential of a Se atom in the dimer.

Table S3. Parameters of two layered (4×4×1) supercells for Se-substituted MoSe$_x$ and WSe$_x$ models.

(a) MoSe$_x$

x	Phase	a, b, c (Å)	α, β, γ (°)	E_{rel}^{tot} (eV)[a]	E_{rel} (meV)[b]	E_{VM} (eV)[c]	E_{sub} (eV)[d]
2.2	2H	13.33, 12.90	90, 90, 120	0	0	5.74	4.47
		13.33, 12.91	90, 90, 120	0.00	0.0		
	2M	12.07, 13.58, 13.22	90, 113.75, 90	6.60	68.7	3.18	2.16
		12.09,13.48, 13.32	90, 113.83, 90	6.85	71.4		
	1T′	13.80, 13.43, 12.42	90, 90, 119	7.26	75.6	3.23	2.17
		13.82,13.44,12.39	90, 90, 119	7.37	76.8		
	T$_d$	12.01, 13.40, 12.57	90, 90, 90	6.91	72.0	3.06	2.48
		12.02,13.35, 12.64	90, 90, 90	6.97	72.6		
2.43	2H	13.40, 12.90	90, 90, 120	0	0		
		13.39, 12.94	90, 90, 120	0.15	1.6		
	2M	12.13, 13.69, 13.27	90, 113.93, 90	3.44	35.8		
		12.13, 13.69, 13.23	90, 113.98, 90	3.50	36.5		
	1T′	13.95, 13.60, 12.29	90, 90, 119	4.06	42.3		
		13.94,13.52, 12.39	90, 90, 119	4.51	46.9		
	T$_d$	12.09, 13.66, 12.36	90, 90, 90	3.50	36.4		
		12.10,13.67,12.36	90, 90, 90	3.63	37.8		

(b) WSe$_x$

x	Phase	a, b, c (Å)	α, β, γ (°)	E_{rel}^{tot} (eV)[a]	E_{rel} (meV)[b]	E_{VM} (eV)[c]	E_{sub} (eV)[d]
2.2	2H	13.31, 12.92	90, 90, 120	0	0	5.19	3.70
		13.34, 12.91	90, 90, 120	0.03	0.3		
	2M	11.98, 13.43, 13.69	90, 112.22, 90	6.52	67.9	2.85	2.01
		12.00, 13.46, 13.70	90, 112.22, 90	6.54	68.1		
	1T′	13.76, 13.45, 12.70	90, 90, 119	7.00	72.9	2.87	1.86
		13.73, 13.40, 12.79	90, 90, 119	7.15	74.5		
	T$_d$	11.97, 13.41, 12.78	90, 90, 90	6.45	67.2	2.77	2.11
		11.98, 13.42, 12.77	90, 90, 90	6.48	67.5		
2.43	2H	13.38, 12.96	90, 90, 120	0	0		
		13.37, 13.02	90, 90, 120	0.16	1.7		
	2M	12.05, 13.72, 13.57	90, 112.99, 90	2.39	24.9		
		12.07, 13.71, 13.53	90, 112.79, 90	2.41	25.1		
	1T′	13.88, 13.69, 12.54	90, 90, 119	3.04	31.6		
		13.90, 13.56, 12.62	90, 90, 119	3.42	35.6		
	T$_d$	12.04, 13.68, 12.59	90, 90, 90	2.33	24.3		
		12.02, 13.60, 12.66	90, 90, 90	2.63	27.4		

[a] Relative total energy of the supercell, defined as $E_{2M \text{ (or 1T′, Td)}} - E_{2H}$.

[b] Relative energy per atoms, defined as E_{rel}^{tot} divided by the number of atoms.

[c] Vacancy energy of metal atoms (per vacancy), defined as $E_{VM} = [E(MoSe_x \text{ or } WSe_x) + n\mu(Mo \text{ or } W) - E(MoSe_2 \text{ or } WSe_2)]/n$ for the metal removal reaction of $MoSe_2$ (or WSe_2) $\rightarrow MoSe_x$

(or WSe_x) + nMo (or nW). E is the total energy of the model, n is the number of vacant metal atoms, and μ(metal) is the chemical potential of a metal atom in the body-centered cubic crystal.

[d] Metal substitution energy per metal, defined as E_{sub} = [E($MoSe_x$ or WSe_x) + $n\mu$(Mo or W) – E($MoSe_2$ or WSe_2) – $n\mu$(Se)]/n for the reaction of $MoSe_2$ (or WSe_2) + nSe → $MoSe_x$ (or WSe_x) + nMo (or W). E is the total energy of the model, μ(metal) is the chemical potential of a metal atom in the body-centered cubic crystal, n is the number of substituted metal or Se atoms, and μ(Se) is the chemical potential of a Se atom in the dimer.

Table S4. Parameters of two layered (4×4×1) supercells for Se-intercalated-substituted $MoSe_{2.33}$ and $WSe_{2.33}$.

	Phase	a, b, c (Å)	α, β, γ (°)	E_{rel}^{tot} (eV)[a]	E_{rel} (meV)[b]	E_{int} (eV)[c]	E_{sub} (eV)[d]
$MoSe_{2.33}$	2H	13.36, 14.79	90, 90, 120	0	0	0.71	3.32
		13.36, 14.92	90, 90, 120	0.46	4.6	0.83	
	2M	12.08, 13.47, 15.25	90, 114.47, 90	3.88	38.9	0.03	1.88
		12.02, 13.56, 14.89	90, 113.96, 90	4.44	43.5	0.09	
	1T′	13.68, 13.52, 14.07	90, 90, 119	4.95	49.5	0.13	2.31
	T_d	12.00, 13.50, 14.08	90, 90, 90	4.13	41.3	0.01	1.71
		12.05, 13.47, 13.93	90, 90, 90	4.72	47.6	0.16	
$WSe_{2.33}$	2H	13.33, 15.28	90, 90, 120	0	0	1.29	3.08
		13.31, 15.02	90, 90, 120	0.48	4.8	1.40	
	2M	12.01, 13.53, 15.25	90, 112.87, 90	1.98	19.8	0.15	1.73
		12.04, 13.51, 14.75	90, 103.49, 9	2.70	27.0	0.33	
	1T′	13.74, 13.53, 14.12	90, 90, 119	3.30	33.0	0.37	2.06
	T_d	12.03, 13.51, 14.05	90, 90, 90	2.63	26.3	0.34	1.69
		12.03, 13.55, 13.73	90, 90, 90	3.29	32.9	0.50	

[a] Relative total energy of the supercell, defined as $E_{2M \text{ (or 1T′, Td)}} - E_{2H}$.

[b] Relative energy per atoms, defined as E_{rel}^{tot} divided by the number of atoms.

[c] Se intercalation energy (per Se), defined by $E_{int} = [E(MoSe_{2.33} \text{ or } WSe_{2.33}) - E(MoSe_{2.2} \text{ or } WSe_{2.2}) - 4\mu(Se)]/4$ for the Se intercalation reaction of $MoSe_{2.2}$ (or $WSe_{2.2}$) + 4Se → $MoSe_{2.33}$ (or $WSe_{2.33}$). The E is the total energies of models and $\mu(Se)$ is the chemical potential of a Se atom in the dimer.

[d] Metal substitution (per metal), defined by $E_{sub} = [E(MoSe_{2.33} \text{ or } WSe_{2.33}) + 2\mu(Mo \text{ or } W) - E(MoSe_{2.13} \text{ or } WSe_{2.13}) - 2\mu(Se)]/2$ for the substitution reaction of $MoSe_{2.13}$ (or $WSe_{2.13}$) + 2Se → $MoSe_{2.33}$ (or $WSe_{2.33}$) + 2Mo (or W). The E is the total energies of models and $\mu(metal)$ is the chemical potential of a metal atom in the body centered cubic crystal.

Table S5. Comparison of HER performance (at 0.5 M H_2SO_4, otherwise specified by *) of 1T (or 1T') phase or selenide TMD samples in the literatures.

Ref. No.	Materials	$\eta_{J=10}$ (mV)	Tafel slope (mV dec^{-1})	TOF (H_2 s^{-1}) at η
S8	$NiSe_2$-Ni_2P/nickel foam	102 (1M KOH)*	68 (1M KOH)*	
S9	$RuSe_2$@NC	30 (1M KOH)*	32 (1M KOH)*	0.57 at 0.15 V
S10	Os-$OsSe_2$	26 23 (1M KOH)*	31	
S11	$Mo_{0.7}V_{0.3}Se_2$ $Mo_{0.6}V_{0.4}Se_2$	114 157 (1M KOH)*	43 76 (1M KOH)*	3.91 at 0.15 V
S12	1T-MoS_2	255	44	
S13	1T-2H MoS_2/ N-rGO quantum-dot	97	39	
S14	Ni (9%)-doped 1T/2H MoS_2	127	86	
S15	1T' $MoSe_{2.25}$	130	46	
S16	Exfoliated 1T WS_2	250	60	175 at 288 mV
S17	Colloidal 1T WS_2	200	50.4	
S18	1T' phase WSe_2 (colloidal)	510	150	
S19	1T WSe_2 on substrate by heating up method	197	143	
S20	$W_{0.9}V_{0.1}Se_2$	128	80	183.3 at 128 mV
This work	2M phase $MoSe_2$	139	70	
This work	2M phase WSe_2	130	74	

MoSe$_{2.06}$			
2H	2M	1T'	T$_d$

	2H	2M	1T'	T$_d$
top				
side				
E$_{rel}$	0	81.8 meV	90.5 meV	86.6 meV

MoSe$_{2.13}$			
2H	2M	1T'	T$_d$

	2H	2M	1T'	T$_d$
top				
side				
E$_{rel}$	0	67.5 meV	69.7 meV	73.3 meV

MoSe$_{2.25}$			
2H	2M	1T'	T$_d$

	2H	2M	1T'	T$_d$
top				
side				
E$_{rel}$	0	29.2 meV	45.8 meV	30.7 meV
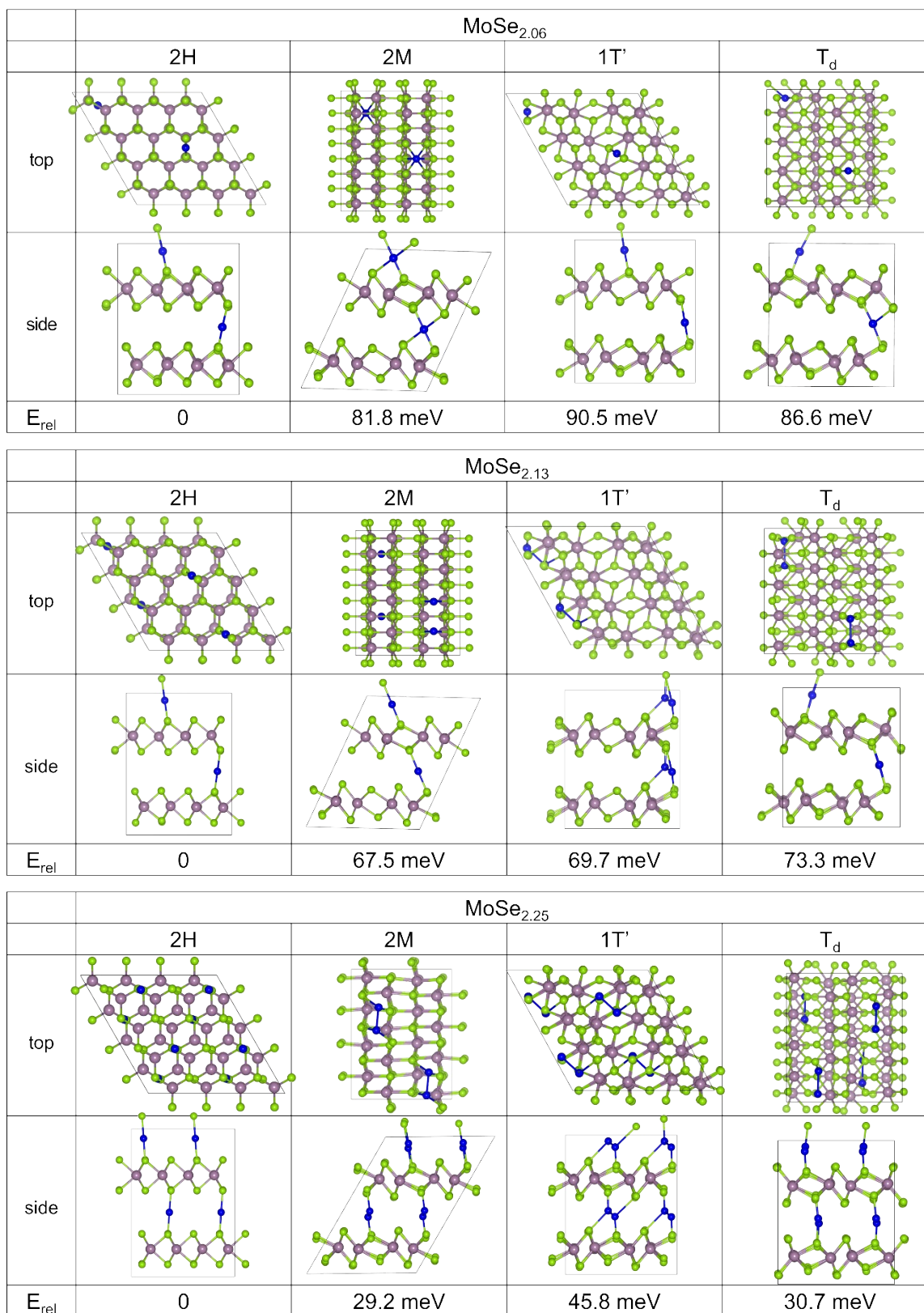
Figure S1. Configurations for Model I of MoSe$_x$ at x = 2.06, 2.13, and 2.25, which were built from (4 × 4 × 1) supercell with two layers. Purple and green balls represent Mo and Se atoms, respectively. The blue balls represent the intercalated Se atoms between layers. The relative energy (E$_{rel}$) per atom is with respect to the most stable phase (2H).

	WSe$_{2.06}$			
	2H	2M	1T'	T$_d$
top				
side				
E$_{rel}$	0	66.1 meV	74.3 meV	71.2 meV

	WSe$_{2.13}$			
	2H	2M	1T'	T$_d$
top				
side				
E$_{rel}$	0	46.8 meV	53.5 meV	54.1 meV

	WSe$_{2.25}$			
	2H	2M	1T'	T$_d$
top				
side				
E$_{rel}$	0	24.7 meV	35.0 meV	16.8 meV
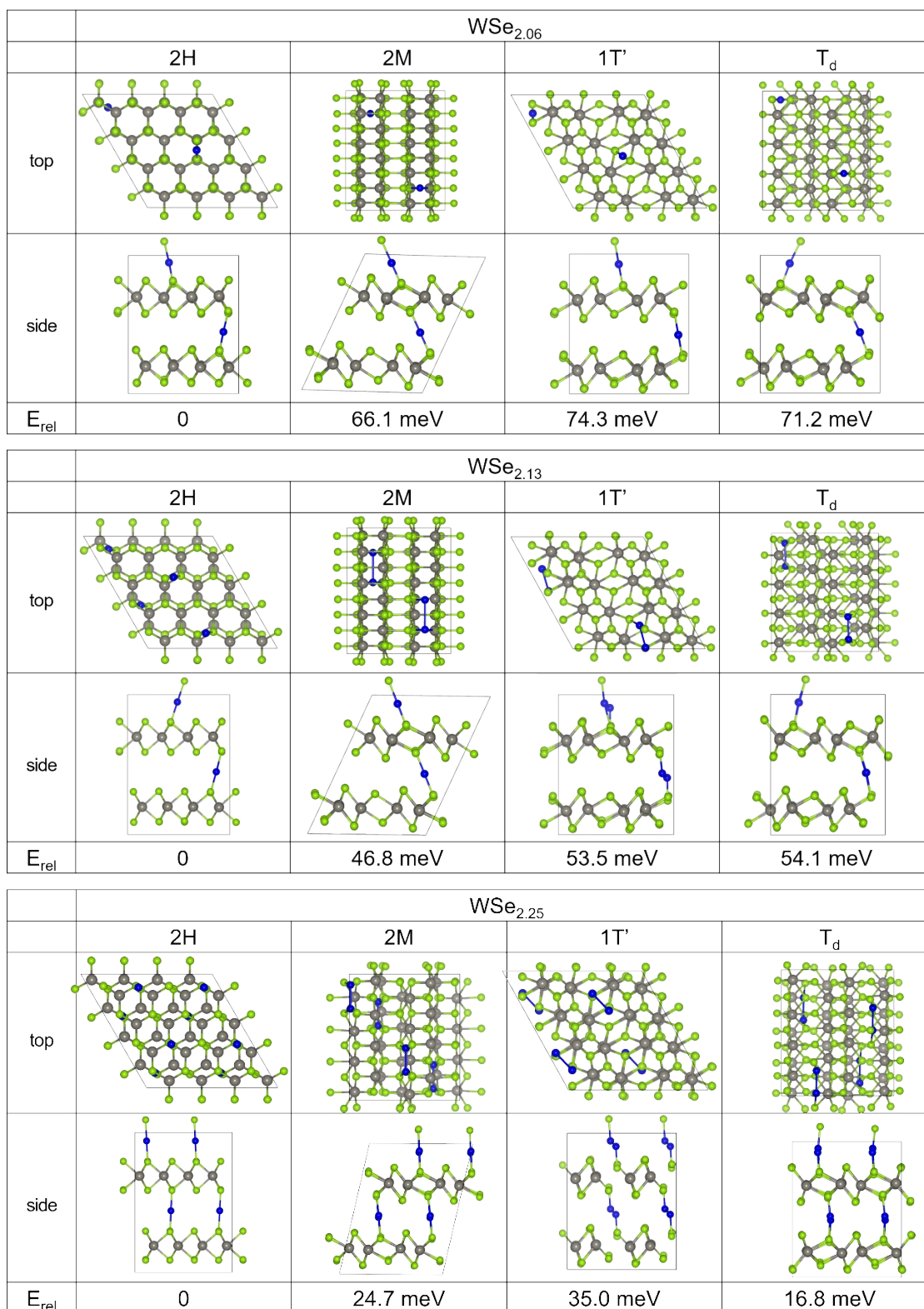
Figure S2. Configurations for Model I of WSe$_x$ at x = 2.06, 2.13, and 2.25, which were built from (4 × 4 × 1) supercell with two layers. Grey and green balls represent W and Se atoms, respectively. The blue balls represent the intercalated Se atoms between layers. The relative energy (E$_{rel}$) per atom is with respect to the most stable phase (2H).

	MoSe$_{2.2}$			
	2H		2M	
top				
E$_{rel}$	0	0.03 meV	68.7 meV	71.4 meV
	1T'		T$_d$	
top				
E$_{rel}$	75.6 meV	76.8 meV	72.0 meV	72.6 meV

	MoSe$_{2.43}$			
	2H		2M	
top				
E$_{rel}$	0	1.6 meV	35.8 meV	36.5 meV
	1T'		T$_d$	
top				
E$_{rel}$	42.3 meV	46.9 meV	36.4 meV	37.8 meV

Figure S3. Configurations for Model S of MoSe$_x$ at x = 2.2 and 2.43, which were built from (4 × 4 × 1) supercell with two layers. Purple and green balls represent Mo and Se atoms, respectively. The orange balls represent the substituted Se atoms at the Mo sites. The orange balls at the bottom layers are marked by dotted circles. The relative energy (E$_{rel}$) per atom is with respect to the most stable phase (2H).
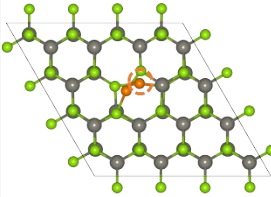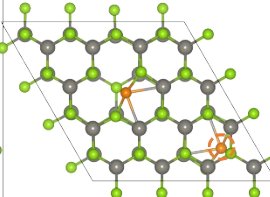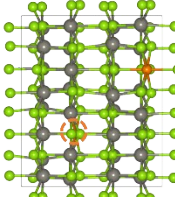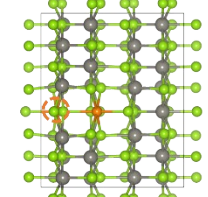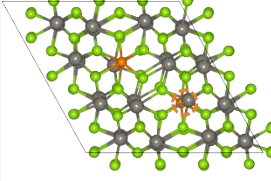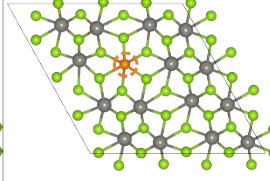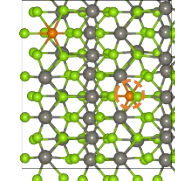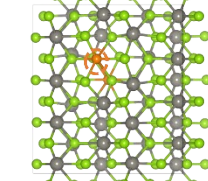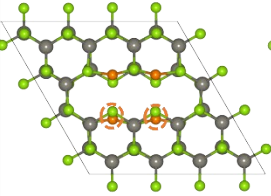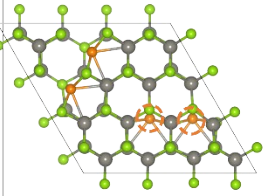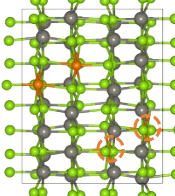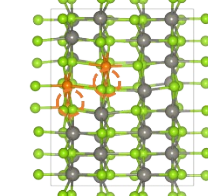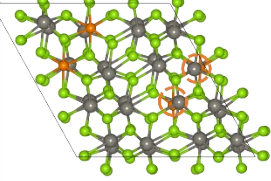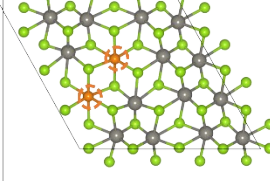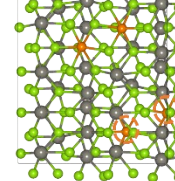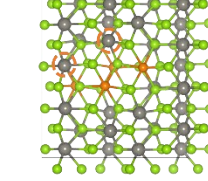
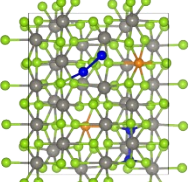|	WSe$_{2.2}$			
	2H		2M	
top				
E$_{rel}$	0	0.3 meV	67.9 meV	68.1 meV
	1T'		T$_d$	
top				
E$_{rel}$	72.9 meV	74.5 meV	67.2 meV	67.5 meV

	WSe$_{2.43}$			
	2H		2M	
top				
E$_{rel}$	0	1.7 meV	24.9 meV	25.1 meV
	1T'		T$_d$	
top				
E$_{rel}$	31.6 meV	35.6 meV	24.3 meV	27.4 meV

Figure S4. Configurations for Model S of WSe$_x$ at x = 2.2 and 2.43, which were built from (4× 4 × 1) supercell with two layers. Gray and green balls represent W and Se atoms, respectively. The orange balls represent the substituted Se atoms at the W sites. The orange balls at the bottom layers are marked by dotted circles. The relative energy (E$_{rel}$) per atom is with respect to the most stable phase (2H).

.

MoSe$_{2.33}$			
2H		2M	
top			
side			
E$_{rel}$	0	4.6 meV	38.9 meV	43.5 meV
1T'		T$_d$	
top			
side			
E$_{rel}$	49.5 meV	41.3 meV	47.6 meV
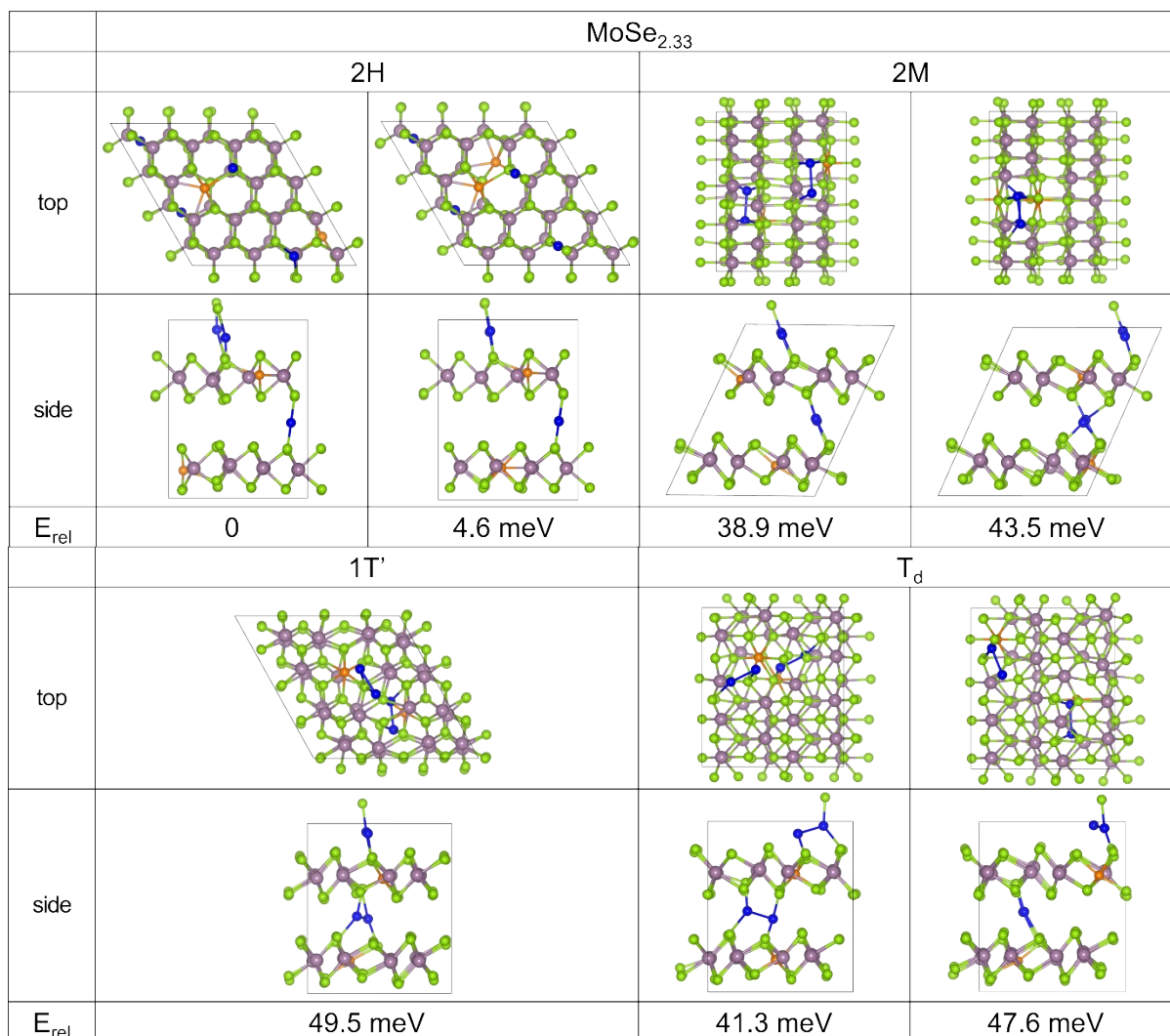
Figure S5. Configurations for Model C of MoSe$_x$ at x = 2.33, which were built from (4 × 4 × 1) supercell with two layers. Purple and green balls represent Mo and Se atoms, respectively. The blue and orange balls represent the intercalated Se atoms between layers and the substituted Se atoms at the Mo sites, respectively. The relative energy (E$_{rel}$) per atom is with respect to the most stable phase (2H).
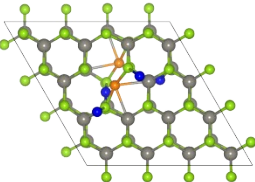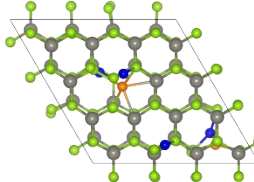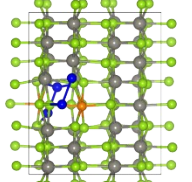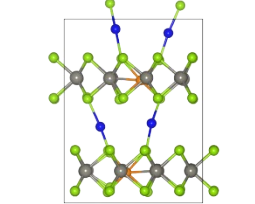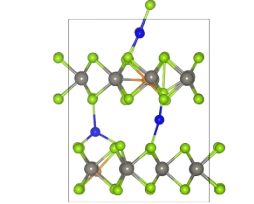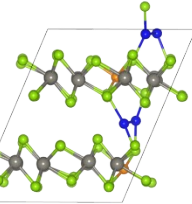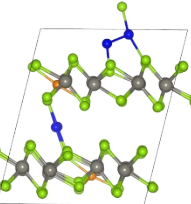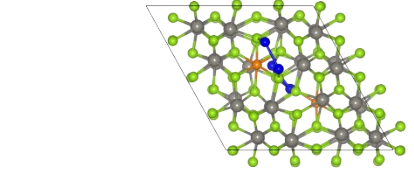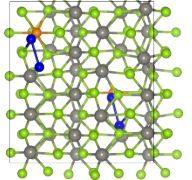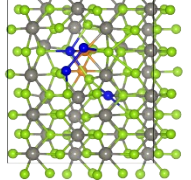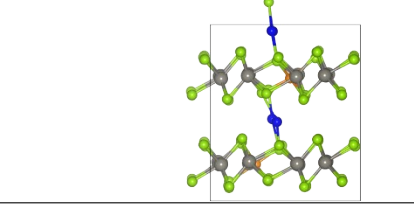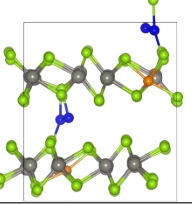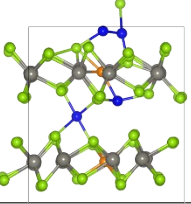
|	WSe$_{2.33}$			
	2H		2M	
top				
side				
E$_{rel}$	0	4.8 meV	19.8 meV	27.0 meV
	1T'		T$_d$	
top				
side				
E$_{rel}$	33.0 meV		26.3 meV	32.9 meV

Figure S6. Configurations for C model of WSe$_x$ at x = 2.33, which were built from (4 × 4 × 1) supercell with two layers. Grey and green balls represent W and Se atoms, respectively. The blue and orange balls represent the bridged Se atoms between layers and the substituted Se atoms at the W sites, respectively. The relative energy (E$_{rel}$) per atom is with respect to the most stable phase (2H).
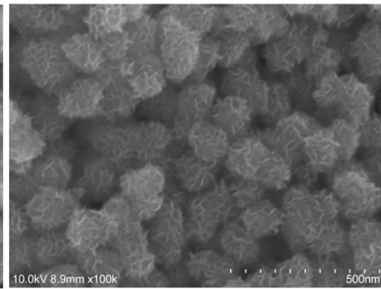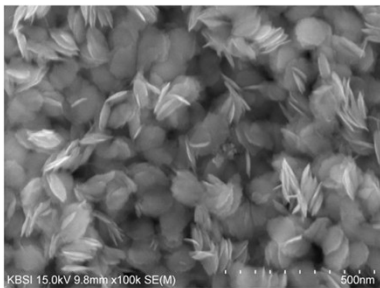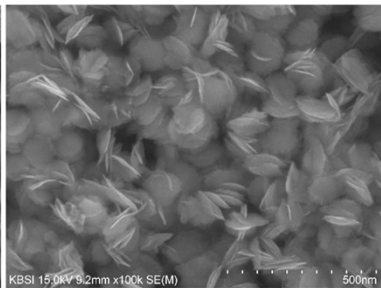
MoSe$_2$
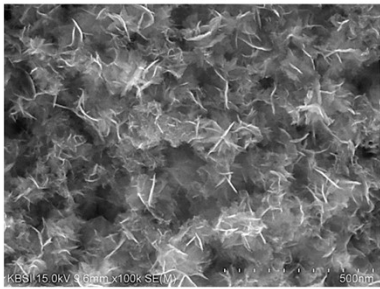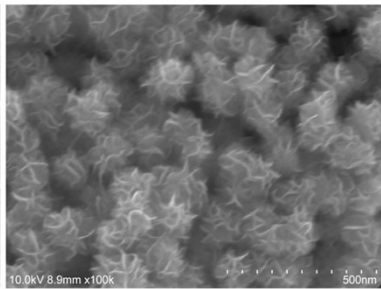
MA	M1	M4

WSe$_2$

WA	W1	W2
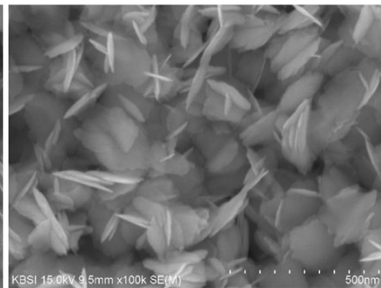
M1
MoSe$_{2.01}$

Element	Series type	Atomic %
Se	L series	67.79
Mo	L series	32.21
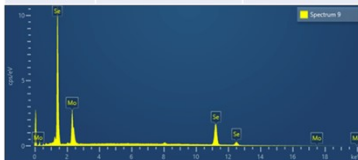
M2
MoSe$_{2.10}$

Element	Series type	Atomic %
Se	L series	67.84
Mo	L series	32.16
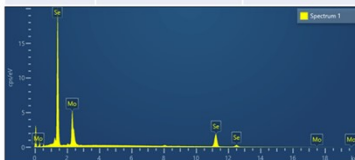
M4
MoSe$_{2.29}$

Element	Series type	Atomic %
Se	L series	69.15
Mo	L series	30.85
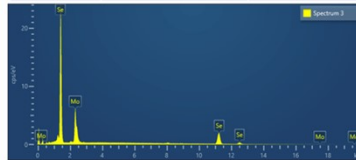
W1
WSe$_{2.05}$

Se	L series	67.29%
W	M series	32.71%
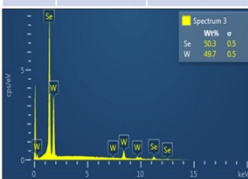
W1.5
WSe$_{2.16}$

Se	L series	68.45%
W	M series	31.55%

W2
WSe$_{2.21}$

Se	L series	68.86%
W	M series	31.14%

W3
WSe$_{2.35}$

Se	L series	70.18%
W	M series	29.82%
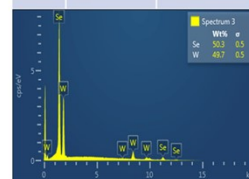
M1 — MoSe$_{2.0}$
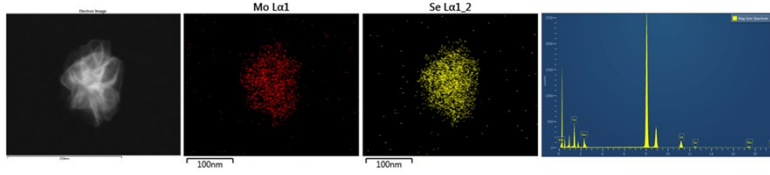
Mo Lα1 Se Lα1_2
100nm 100nm

Element	Line Type	k Factor	Absorption Correction	Wt%	Wt% Sigma	Atomic %
Se	L series	1.703	1.00	62.13	1.60	66.59
Mo	L series	1.790	1.00	37.87	1.60	33.41
Total:				100.00		100.00

M1.5 — MoSe$_{2.05}$
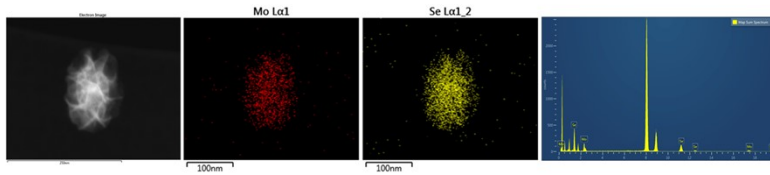
Mo Lα1 Se Lα1_2
100nm 100nm

Element	Line Type	k Factor	Absorption Correction	Wt%	Wt% Sigma	Atomic %
Se	L series	1.703	1.00	62.81	1.67	67.21
Mo	L series	1.790	1.00	37.19	1.67	32.79
Total:				100.00		100.00

M2 — MoSe$_{2.15}$
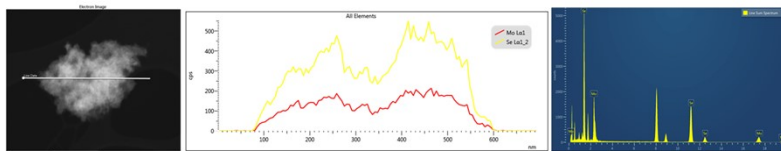
All Elements — Mo Lα1, Se Lα1_2

Element	Line Type	k Factor	Absorption Correction	Wt%	Wt% Sigma	Atomic %
Se	L series	1.703	1.00	63.89	1.67	68.22
Mo	L series	1.790	1.00	36.11	1.67	31.78
Total:				100.00		100.00
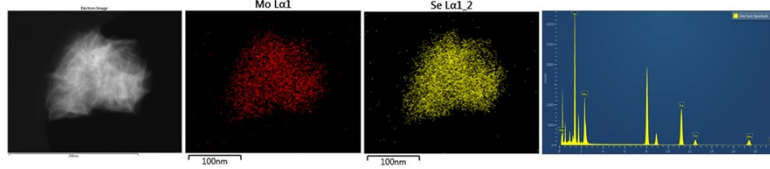
M3 — MoSe$_{2.21}$

Mo Lα1 Se Lα1_2
100nm 100nm

Element	Line Type	k Factor	Absorption Correction	Wt%	Wt% Sigma	Atomic %
Se	L series	1.703	1.00	64.53	0.59	68.85
Mo	L series	1.790	1.00	35.47	0.59	31.15
Total:				100.00		100.00

M3.5 — MoSe$_{2.26}$
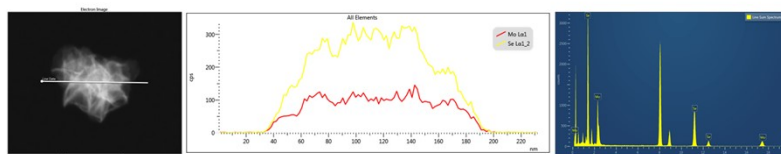
All Elements — Mo Lα1, Se Lα1_2

Element	Line Type	k Factor	Absorption Correction	Wt%	Wt% Sigma	Atomic %
Se	L series	1.703	1.00	65.01	0.60	69.30
Mo	L series	1.790	1.00	34.99	0.60	30.70
Total:				100.00		100.00

M4 — MoSe$_{2.30}$
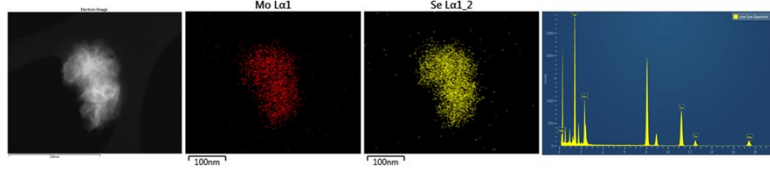
Mo Lα1 Se Lα1_2
100nm 100nm

Element	Line Type	k Factor	Absorption Correction	Wt%	Wt% Sigma	Atomic %
Se	L series	1.703	1.00	65.35	0.63	69.62
Mo	L series	1.790	1.00	34.65	0.63	30.38
Total:				100.00		100.00
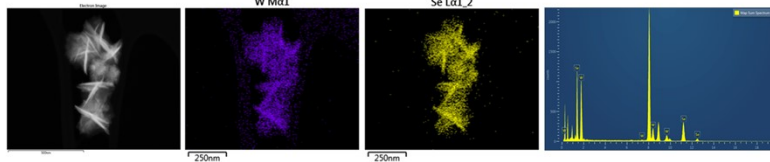
W1 — WSe$_{2.03}$

W Mα1 Se Lα1_2
250nm 250nm

Element	Line Type	k Factor	Absorption Correction	Wt%	Wt% Sigma	Atomic %
Se	L series	1.703	1.00	46.56	0.89	66.98
W	M series	1.589	1.00	53.44	0.89	33.02
Total:				100.00		100.00

W1.5 — WSe$_{2.11}$
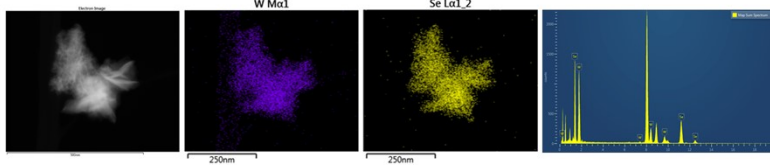
W Mα1 Se Lα1_2
250nm 250nm

Element	Line Type	k Factor	Absorption Correction	Wt%	Wt% Sigma	Atomic %
Se	L series	1.703	1.00	47.50	0.79	67.81
W	M series	1.589	1.00	52.50	0.79	32.19
Total:				100.00		100.00

W2 — WSe$_{2.20}$
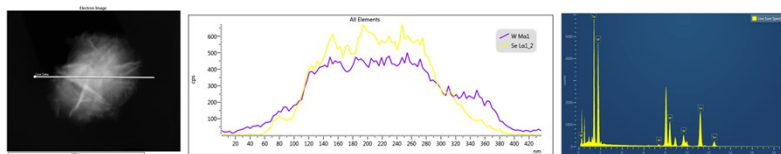
All Elements — W Mα1, Se Lα1_2

Element	Line Type	k Factor	Absorption Correction	Wt%	Wt% Sigma	Atomic %
Se	L series	1.703	1.00	48.55	0.38	68.72
W	M series	1.589	1.00	51.45	0.38	32.28
Total:				100.00		100.00

W3 — WSe$_{2.27}$
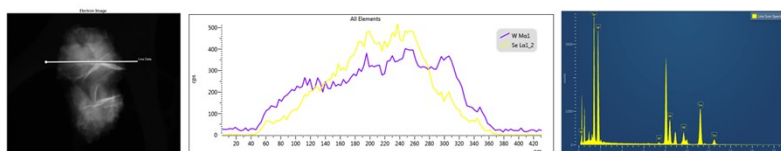
All Elements — W Mα1, Se Lα1_2

Element	Line Type	k Factor	Absorption Correction	Wt%	Wt% Sigma	Atomic %
Se	L series	1.703	1.00	49.37	0.48	69.45
W	M series	1.589	1.00	50.63	0.48	30.55
Total:				100.00		100.00
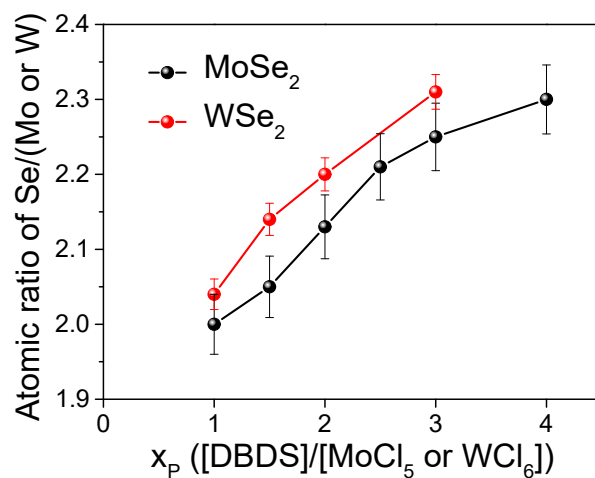
Figure S7. SEM images and corresponding energy-dispersive X-ray spectroscopy (EDX) data, scanning transmission electron microscopy (STEM) image, and EDX (elemental mapping and line profiles) data for $MoSe_2$ and WSe_2 samples. The atomic ratio of Se/Mo (or Se/W) is plotted as a function of the molar ratio of precursors (x_P = [DBDS]/[$MoCl_5$] or [DBDS]/[WCl_6]), showing an increase with increasing x_P. The atomic ratio of Se/metal was obtained using the average of all EDX data.
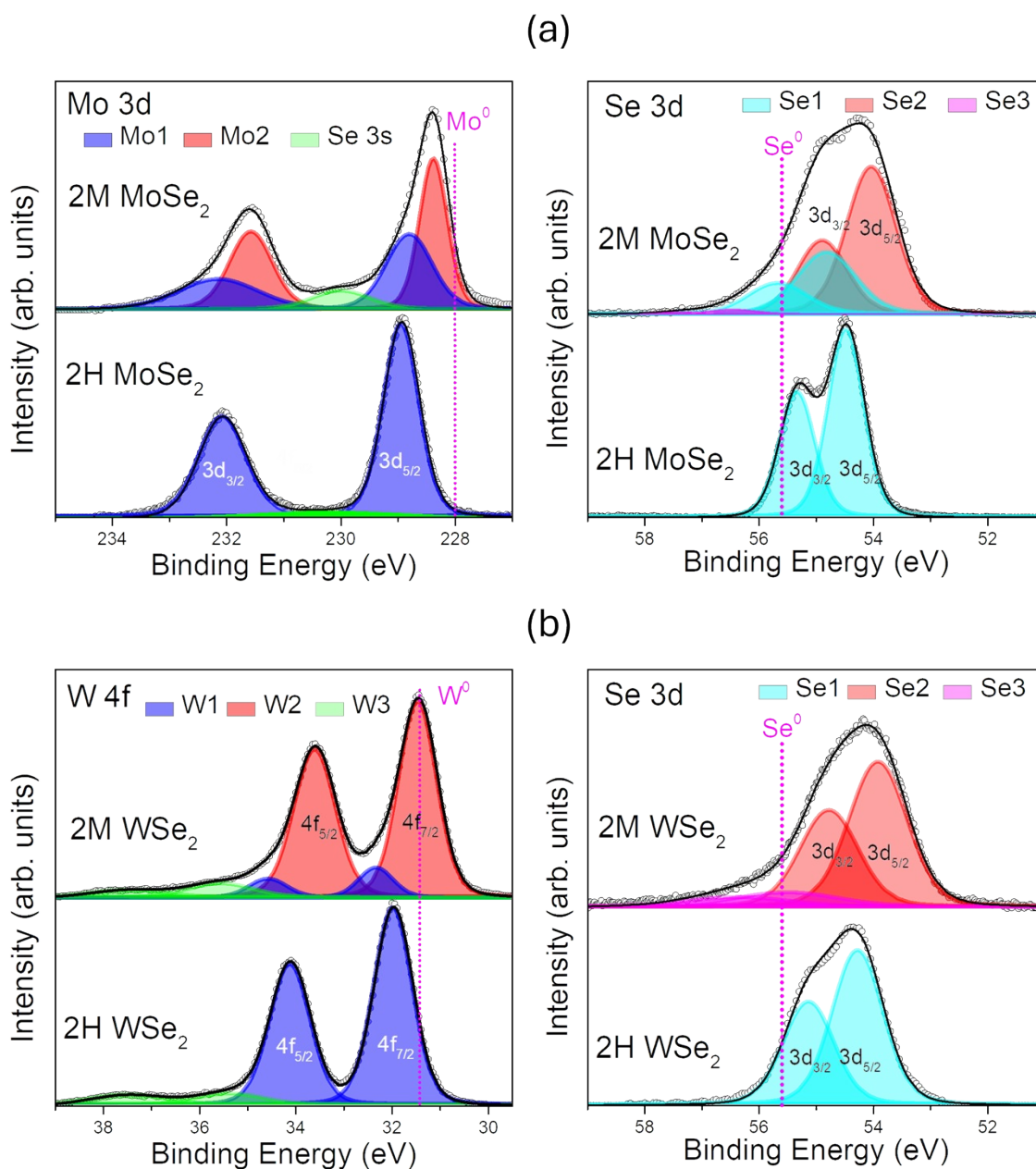
Figure S8. Fine-scan XPS peaks of (a) Mo $3d$ ($3d_{5/2}$ and $3d_{3/2}$) and Se $3d$ ($3d_{5/2}$ and $3d_{3/2}$) of 2H (MA sample) and 2M (M4 samples) phase $MoSe_2$; (b) W $4f$ ($4f_{7/2}$ and $4f_{5/2}$) and Se $3d$ ($3d_{5/2}$ and $3d_{3/2}$) of 2H (WA sample) and 2M (W3 sample) phase WSe_2. Positions of neutral Mo^0 ($3d_{5/2}$ at 228.0 eV), W^0 ($4f_{7/2}$ at 31.4 eV) and Se^0 ($3d_{5/2}$ at 55.6 eV) are marked by dotted vertical lines.

X-ray photoelectron spectroscopy (XPS) was used to investigate the electronic structures of the samples. The fine-scanned peaks were resolved using the Voigt function.

(a) The Mo $3d_{5/2}$ and $3d_{3/2}$ peaks are separated by 3.13 eV. In 2H $MoSe_2$, the Mo $3d_{5/2}$ peak at 229.0 eV (1.0 eV blue shifted from neutral Mo at 228.0 eV) corresponds to the 2H phase Mo-Se bonding structures. In 2M $MoSe_2$, the peak redshifts to 228.5 eV, indicating that the Mo-Se bond become more metallic than that of 2H $MoSe_2$. The peak was resolved into two bands (Mo1 at 228.8 eV and Mo2 at 228.3 eV for $3d_{5/2}$), which are originated from the 2H and 2M

phase Mo-Se bonding structures, respectively. The ratio of 2M:2H is 62:38, indicating that the main phase is 2M. The Se 3s peak of 2H and 2M MoSe$_2$ appears at 230.5 and 230.0 eV with 1.5 and 2 eV redshift from neutral Se (232 eV), respectively. The intensity of Se 3s peak is larger for 2M phase, indicating that the 2M phase contains more Se atoms than the 2H phase.

The Se 3$d_{5/2}$ and 3$d_{3/2}$ peaks are separated by 0.86 eV. The 2H and 2M phases show the Se 3$d_{5/2}$ peak at 54.5 and 54.2 eV, respectively, which are redshifted by 1.1 and 1.4 eV with respect to the Se^0 signal (55.6 eV). In 2M MoSe$_2$, the peak was resolved three bands (Se1 at 54.8 eV, Se2 at 54.0 eV, and Se3 at 56.4 eV). The Se1 and Se2 bands correspond to Se^{2-} anions bonded to the 2H and 2M phase Mo cations. The Se3 band is assigned to the Se–Se bonds originated from excess Se atoms. XPS analysis confirmed that the 2M phase MoSe$_2$ is more metallic than the 2H phase and enriched with the Se atoms.

(b) The W 4$f_{7/2}$ and 4$f_{5/2}$ peaks are separated by 2.18 eV. For 2H phase WSe$_2$, the W 4$f_{7/2}$ peak at 32.0 eV (blue-shifted by 0.6 eV from neutral W at 31.4 eV) is assigned to the 2H phase W–Se bonding structures (denoted as the W1 band). The 4$f_{7/2}$ peak at 35.5 eV (denoted as the W3 band) corresponds to the bonding structures of W^{6+} and O at the surface layers. The 2M WSe$_2$ shows the W 4$f_{7/2}$ peak (denoted as the W2 band) at 31.4 eV (close to neutral W) that corresponds to the metallic 2M phase. In addition to the W3 band (W–O) at 35.5 eV, the W1 band at 32.2 eV is ascribed to the residual 2H phase. The WSe$_2$ samples appear to be more oxidized than the MoSe$_2$ samples.

The 2H and 2M phases show the Se 3$d_{5/2}$ peak at 54.2 and 53.9 eV, respectively, which are redshifted by 1.4 and 1.7 eV with respect to the Se^0 signal (55.6 eV). These bands (Se1 at 54.3 eV and Se2 at 53.8 eV) correspond to Se^{2-} anions bonded to the 2H and 2M phase W cations, respectively. The Se3 band (55.6 eV) observed for 2M WSe$_2$ are assigned to the Se–Se bonds originated from excess Se atoms. XPS analysis confirmed that the 2M phase WSe$_2$ is more metallic than the 2H and enriched with the Se atoms.
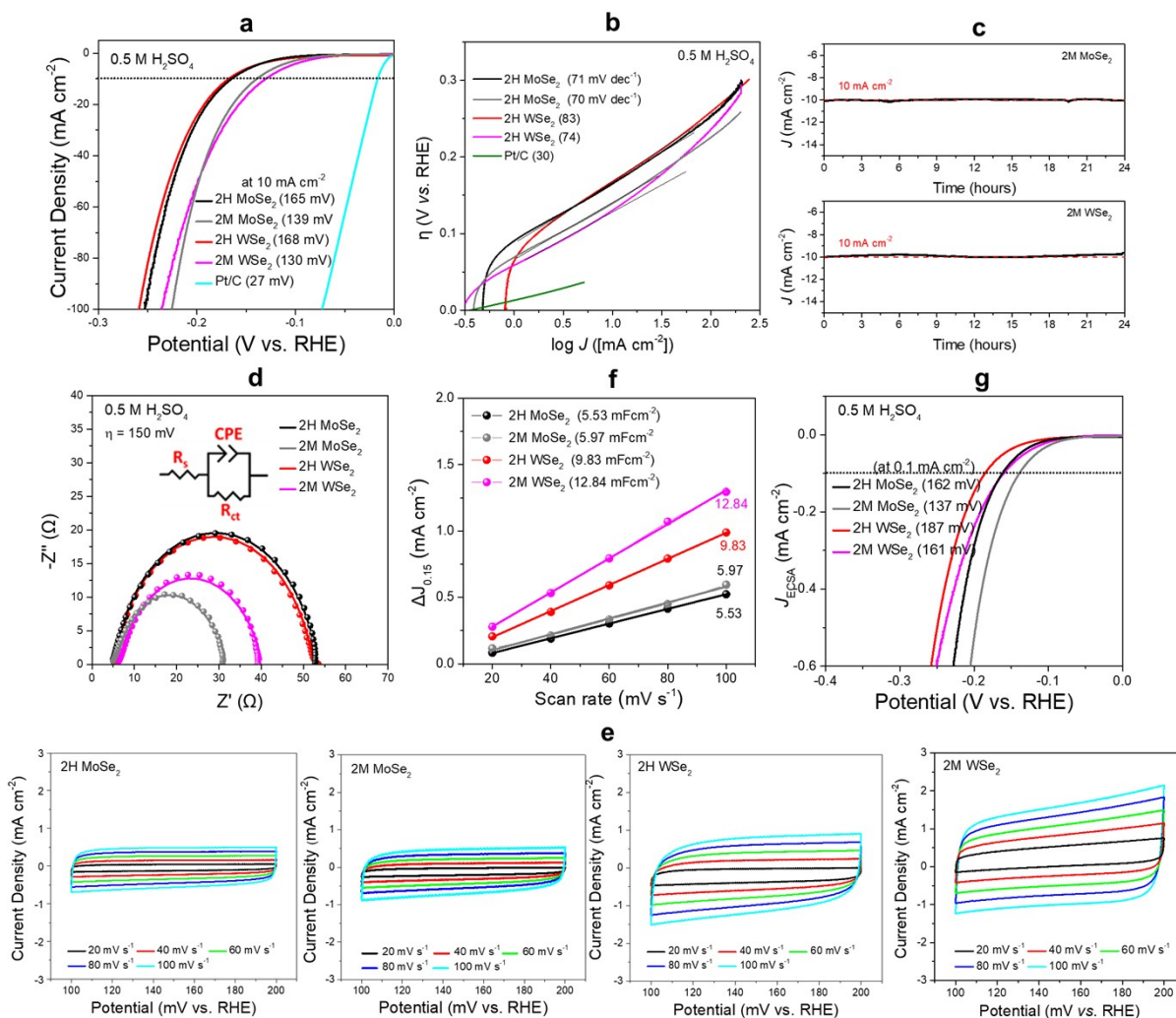
.

Figure S9. HER performance of MoSe$_2$ (2H phase MA and 2M phase M3) and WSe$_2$ (2H phase WA and 2M phase W2) nanosheets.

(a) Linear sweep voltammetry (LSV) curves of Pt/C, MA (denoted as 2H MoSe$_2$), and M3 (denoted as 2M MoSe$_2$), and WA (denoted as 2H WSe$_2$), and W2 (denoted as 2M WSe$_2$). The current density (in mA cm^{-2}) corresponds to the measured current (J) divided by the electrode area (0.1963 cm^2), and is plotted as a function of applied potential *vs.* reversible hydrogen electrode (RHE), which is equal to the overpotential (η). The η to deliver 10 mA cm^{-2} is denoted as $\eta_{J=10}$. The 2M phase exhibits the lower $\eta_{J=10}$ than that of 2H phase; 165 mV (2H MoSe$_2$), 139 mV (2M MoSe$_2$), 168 mV (2H WSe$_2$), 130 mV (2M WSe$_2$). For comparison, $\eta_{J=10}$ = 27 mV was obtained for commercial 20 wt.% Pt/C catalyst.

(b) Tafel plots (η *vs.* log J), which are derived from the LSV curves in the range of η = 0–0.3 V. The Tafel plot is based on the equation $\eta = b \log(J/J_0)$, where b is the Tafel slope, and J_0 is the exchange current density (extrapolated value at η = 0). Linear fit provides the b values: 71

mV dec^{-1} (2H MoSe$_2$), 70 mV dec^{-1} (2M MoSe$_2$), 83 mV dec^{-1} (2H WSe$_2$), 74 mV dec^{-1} (2M WSe$_2$). The sample with lower $\eta_{J=10}$ shows a higher J_0. In comparison, commercial 20 wt.% Pt/C catalyst exhibited $b = 30$ mV dec^{-1}.

(c) The stability test of 2M phase using chronoamperometry (CA) measurement showed almost no degradation of currents at $\eta_{J=10}$ for 24 h.

(d) Nyquist plots using the frequency in the range from 100 kHz to 0.1 Hz at a potential of -0.15 V (η = 150 mV). The modified Randles circuit for fitting is shown in the inset. Electrochemical impedance spectroscopy (EIS) measurements of the samples were performed using an amplitude of 10 mV. In the high-frequency limit and under non-Faradaic conditions, the electrochemical system is approximated by the modified Randles circuit shown in the inset, where R_s denotes the solution resistance, CPE is a constant-phase element related to the double-layer capacitance, and R_{ct} is the charge-transfer resistance from any residual Faradaic processes. A semicircle in the low-frequency region of the Nyquist plots represents the charge transfer process, with the diameter of the semicircle reflecting the charge-transfer resistance. The real (Z') and negative imaginary ($-Z''$) components of the impedance are plotted on the x and y axes, respectively. The simulation of the EIS spectra using an equivalent circuit model allowed us to determine the charge transfer resistance, R_{ct}, which is a key parameter for characterizing the catalyst-electrolyte charge transfer process. The fitting parameters are summarized as follows. A smaller R_{ct} value of 2M phase than of 2H phase indicates more facile electron transfer kinetics that enhances the catalytic activity. The R_{ct} values suggest that the HER performance is determined by the charge transfer rate.

[Fitting Impedance parameters for the equivalent circuit]

Sample	R_s (Ω)	CPE (mF)	R_{ct} (Ω)
2H MoSe$_2$	5.19	0.84	48.16
2M MoSe$_2$	5.26	1.80	26.03
2H WSe$_2$	5.23	1.49	50.45
2M WSe$_2$	6.47	3.15	33.72

(e) Cyclic voltammetry (CV) curves of samples in a non-Faradaic region at 20-100 mV s^{-1} scan rates (with a step of 20 mV s^{-1}). The scan range is 0.1–0.2 V $vs.$ RHE, in 0.5 M H$_2$SO$_4$.

(f) Difference (ΔJ) between the anodic charging and cathodic discharging currents measured at 0.15 V (in 0.5 M H_2SO_4) *vs.* RHE is plotted as a function of the scan rate, and the slope provide the C_{dl} value. Herein, we plotted the half of ΔJ to show directly C_{dl}.

[ECSA of samples calculated using the equation of ECSA = C_{dl}/C_s, where C_s is the flat standard capacitor (60 μF cm⁻²)[S7]]

Sample	C_{dl} (mF cm⁻²)	ECSA
2H MoSe$_2$	5.53	92.17
2M MoSe$_2$	5.97	99.50
2H WSe$_2$	9.83	163.83
2M WSe$_2$	12.84	214.00

(g) Electrochemically active surface area (ECSA) was estimated using C_{dl} (see the experimental section in Supporting Information). The LSV curve was plotted using J_{ECSA} (J divided by ECSA), showing the higher catalytic activity of 2M phase than that of 2H phase.

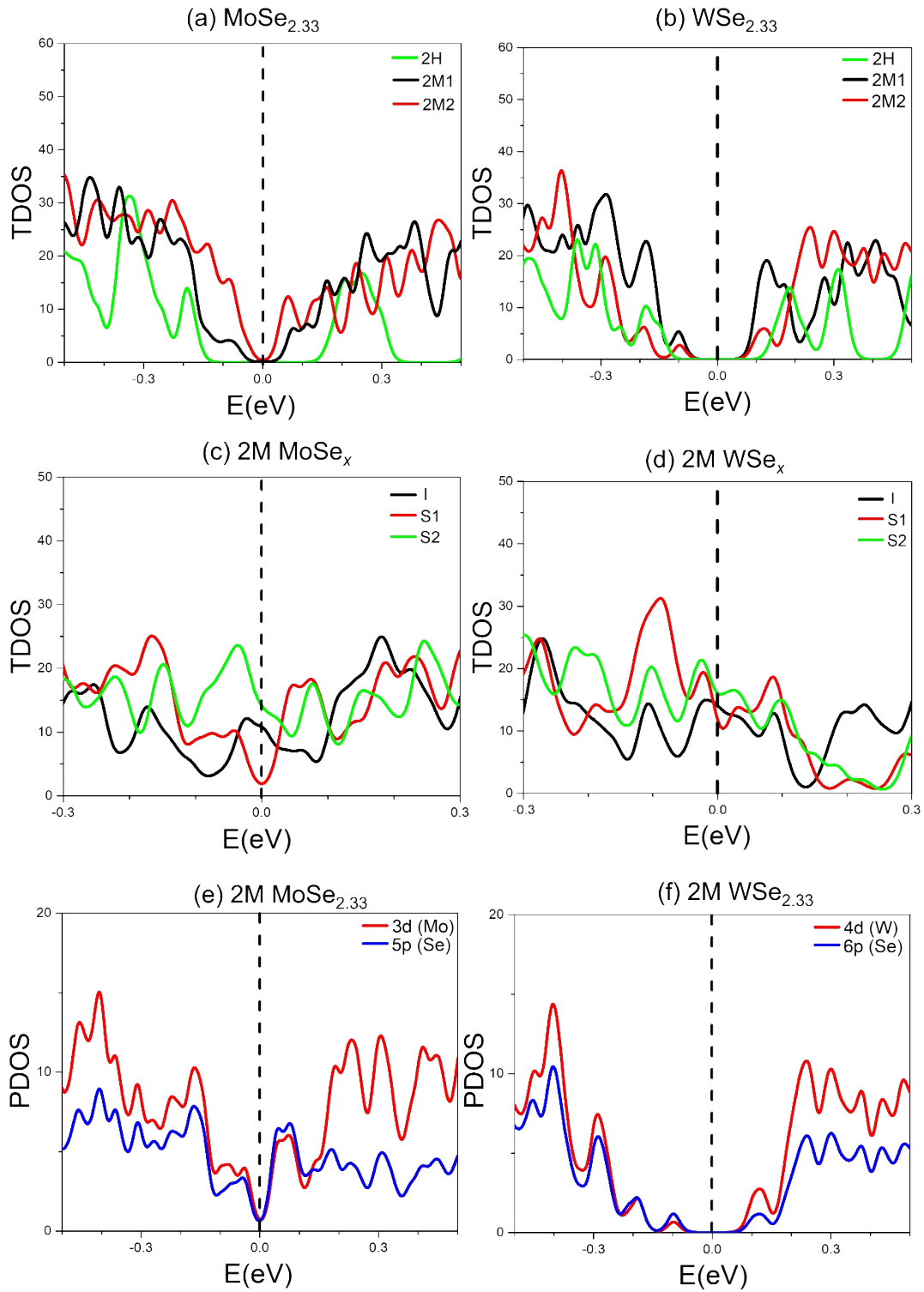**Figure S10**. TDOS of (a) $MoSe_{2.33}$ and (b) $WSe_{2.33}$ (Model C) with the 2H and 2M (2M1 and 2M2) phases; (c) $MoSe_x$ and (d) WSe_x for Model I (at $x = 2.13$) and Model S (S1 and S2 at $x = 2.2$), calculated using the PBE method. PDOS of (e) $MoSe_{2.33}$ and (f) $WSe_{2.33}$ for the 2M1 configuration.

(a), (b) The TDOS of $MoSe_{2.33}$ and $WSe_{2.33}$ for 2H and 2M (2M1 and 2M2) was calculated using the PBE method. The Fermi level (black dashed line) is set to zero. The 2M1 represents the most stable configuration of 2M phase, and 2M2 corresponds to the next stable configuration. The 2M2 is less stable than the 2M1 by 4.6 meV and 7.2 meV for $MoSe_{2.33}$ and $WSe_{2.33}$, respectively. For $MoSe_{2.33}$, 2M1 and 2M2 exhibit the band gap (E_g) of 0.03 and 0.01 eV, respectively. Specifically, 2M2 of $MoSe_{2.33}$ is a semimetal. The 2H phase is a semiconductor with $E_g = 0.18$ eV. For $WSe_{2.33}$, $E_g = 0.09$ eV for both 2M1 and 2M2, and $E_g = 0.21$ eV for the 2H phase. Note that the PBE usually underestimates the band gap.

(c), (d) TDOS of 2M phase for Model I (at $x = 2.13$) and Model S (S1 and S2 at $x = 2.2$) was calculated using the PBE method. The S1 represents the most stable configuration of 2M phase Model S, and S2 corresponds to the next stable configuration. The S2 is less stable than the S1 by 2.7 meV and 0.2 meV for $MoSe_{2.2}$ and $WSe_{2.2}$, respectively. The Model I and S are metallic, which needs further investigation.

(e), (f) Partial DOS (PDOS) of $MoSe_{2.33}$ and $WSe_{2.33}$ was calculated for the 2M1 configuration. The PDOS of d(M) and p(Se) states shows the same feature, indicating that the TDOSs are governed by a strong hybridization near the Fermi level.

References

(S1)   G. Kresse and J. Furthmüller, Efficient iterative schemes for *ab initio* total-energy calculations using a plane-wave basis set. *Phys. Rev. B*, 1996, **54**, 11169−11186.

(S2)   G. Kresse and J. Furthmüller, Efficiency of *ab initio* total-energy calculations for metals and semiconductors using a plane-wave basis set. *Comput. Mater. Sci.*, 1996, **6**, 15−50.

(S3)   P. E. Blöchl, Projector augmented-wave method. *Phys. Rev. B*, 1994, **50**, 17953-17979.

(S4)   S. A. Nosé, Unified formulation of the constant temperature molecular dynamics methods show affiliations. *J. Chem. Phys.*, 1984, **81**, 511−519.

(S5)   J. Mou, Y. Gao, J. Wang, J. Ma and H. Ren, Hydrogen evolution reaction activity related to the facet-dependent electrocatalytic performance of NiCoP from first principles. *RSC Advances*, 2019, **9**, 11755−11761.

(S6)   C. J. Cramer, *Essentials of computational chemistry: theories and models, 2nd Edition*; John Wiley & Sons Ltd.: West Sussex, **2004**; Chapter 10.

(S7)   L. Li, Z. Qin, L. Ries, S. Hong, T. Michel, J. Yang, C. Salameh, M. Bechelany, P. Miele, M. Kaplan, M. Chhowalla and D. Voiry, Role of sulfur vacancies and undercoordinated Mo regions in MoS_2 nanosheets toward the evolution of hydrogen. *ACS Nano*, 2019, **13**, 6824-6834.

(S8)   P. Wang, Z. Pu, W. Li, J. Zhu, C. Zhang, Y. Zhao and S. Mu, Coupling $NiSe_2$-Ni_2P heterostructure nanowrinkles for highly efficient overall water splitting. *J. Catal.*, 2019, **377**, 600-608.

(S9)   D. Chen, R. Lu, Y. Yao, D. Wu, H. Zhao, R. Yu, Z. Pu, P. Wang, J. Zhu, J. Yu, P. Ji, Z. Kou, H. Tang and S. Mu, Duetting electronic structure modulation of Ru atoms in $RuSe_2$@NC enables more moderate H* adsorption and water dissociation for hydrogen evolution reaction. *J. Mater. Chem. A*, 2022, **10**, 7637-7644.

(S10) D. Chen, R. Lu, R. Yu, Y. Dai, H. Zhao, D. Wu, P. Wang, J. Zhu, Z. Pu, L. Chen, J. Yu and S. Mu, Work-function-induced Interfacial Built-in Electric Fields in Os-$OsSe_2$ Heterostructures for Active Acidic and Alkaline Hydrogen Evolution, *Angew. Chem. Int. Ed.*, 2022, **61**, e202208642.

(S11) I. S. Kwon, I. H. Kwak, T. T. Debela, J. Y. Kim, S. J. Yoo, J. -G. Kim, J. Park and H. S. Kang, Phase-transition $Mo_{1-x}V_xSe_2$ alloy nanosheets with rich V−Se vacancies and their enhanced catalytic performance of hydrogen evolution reaction. *ACS Nano* 2021, **15**, 14672-14682.

(S12) H. Li, X. Han, S. Jiang, L. Zhang, W. Ma, R. Ma and Z. Zhen, Controllable fabrication and structure evolution of hierarchical 1T-MoS_2 nanospheres for efficient hydrogen evolution, *Green Energy & Environ.*, 2022, **7**, 314.

(S13) L. Ma, L. Jiang, X. Li, P. Zuo, C. Xu, Z. Cheng, M. Tian, Y. Yuan, X. Zhang, Y. Lu, Y. Zhao and L. Qu, One-step ultrafast laser induced synthesis of strongly coupled 1T-2H MoS_2/ N-rGO quantum-dot heterostructures for enhanced hydrogen evolution, *Chem. Eng. J.*, 2022, **445**, 136618.

(S14) R. K. Dharman, B. M. Francis, J. S. Ponraj, S. C. Dhanabalan, R. K. Manavalan and T. H. Oh, Study on Nickel-induced 1T/2H MoS_2 nanostructures in realizing efficient electrocatalysts for hydrogen evolution reaction, *J. Electroanal. Chem*., 2022, **925**, 116905.

(S15) I. S. Kwon, I. H. Kwak, T. T. Debela, H. G. Abbas, Y. C. Park, J. Ahn, J. Park and H. S. Kang, Se-rich $MoSe_2$ nanosheets and their superior electrocatalytic performance for hydrogen evolution reaction. *ACS Nano*, 2020, **15**, 6925−6304.

(S16) D. Voiry, H. Yamaguchi, J. Li, R. Silva, D. C. B. Alves, T. Fujita, M. Chen, T. Asefa, V. B. Shenoy, G. Eda and M. Chhowalla, M. Enhanced catalytic activity in strained chemically exfoliated WS_2 nanosheets for hydrogen evolution. *Nat. Mater.*, 2013, **12**, 850-855.

(S17) Z. Liu, N. Li, C. Su, H. Zhao, L. Xu, Z. Yin, J. Li and Y. Du, Colloidal synthesis of 1T' phase dominated WS_2 towards endurable electrocatalysis. *Nano Energy*, 2018, **50**, 176-181.

(S18) M. S. Sokolikova, P. C. Sherrell, P. Palczynski, V. L. Bemmer and C. Mattevi, C. Direct solution-phase synthesis of 1T' WSe_2 nanosheets. *Nat. Commun.*, 2019, **10**, 712.

(S19) Y. J. Park, H. S. So, H. Hwang, D. S. Jeong, H. J. Lee, L. Lim, C. G. Kim and H. S. Shin, Synthesis of 1T WSe_2 on an oxygen-containing substrate using a single precursor. *ACS Nano*, 2022, **16**, 11059-11065.

(S20) I. S. Kwon, I. H. Kwak, G. M. Zewdie, S. J. Lee, J. Y. Kim, S. J. Yoo, J. -G. Kim, J. Park and H. S. Kang, WSe_2-VSe_2 alloyed nanosheets to enhance the catalytic performance of hydrogen evolution reaction. *ACS Nano*, 2022, **16**, 12569-12579.